Computation & theory

Stable and metastable structures and their energetics of asymmetric tilt grain boundaries in MgO: a simulated annealing approach

T. Yokoi[1,*] , Y. Kondo[1], K. Ikawa[1], A. Nakamura[1], and K. Matsunaga[1,2]

[1] *Department of Materials Physics, Nagoya University, Nagoya 464-8603, Japan*
[2] *Nanostructures Research Laboratory, Japan Fine Ceramics Center, Nagoya 456-8587, Japan*

ABSTRACT

A simulated annealing (SA) method based on molecular dynamics is employed to reveal atomic structures of asymmetric tilt grain boundaries (ATGBs) in MgO. $\Sigma5$ and $\Sigma13$ ATGBs with the [001] tilt axis are systematically investigated. The ATGBs after SA simulations dissociate into saw-toothed nanofacets composed of multiple structural units. These nanofacets are lower in GB energy than those obtained from a γ-surface method with structural optimization, demonstrating the importance of SA-based methods for obtaining low-energy structures of ATGBs. For most of the $\Sigma5$ ATGBs, the nanofacets consist of only structural units of $\Sigma5$ symmetric tilt GBs (STGBs). For the $\Sigma13$ ATGBs studied, their nanofacets do not consist of only $\Sigma13$ STGBs but always contain non-$\Sigma13$ structural units, which probably results from a large difference between the excess volume of $\Sigma13(510)$ and $\Sigma13(320)$ STGBs. It is also found that ATGBs have a larger number of metastable structures whose GB energies are close to the lowest energy structure than STGBs, due to the fact that ATGB nanofacets are more tolerant of variation in facet junction, structural units and their arrangement. Consequently, the lowest energy structures have low probabilities of being formed than metastable structures.

Introduction

In crystalline materials, grain boundaries (GBs) often govern their macroscopic properties and functionalities, through changing atomic configurations and chemical compositions within a few nanometers from GB planes. It has been reported that physical properties of individual GBs significantly vary with their crystallographic characteristics. For instance, increasing proportions of $\Sigma3$ twin GBs in metals and alloys demonstrated improved resistance to intergranular corrosion and embrittlement [1–5].

Handling Editor: Shen Dillon.

Address correspondence to E-mail: yokoi@mp.pse.nagoya-u.acjp

Springer

Experiments using bicrystal samples also showed that electrical conductivities [6], diffusivities [7, 8] and thermal conductivities along or across GBs strongly depend on individual GB characters [9, 10]. Although such GB properties are known to be well correlated with GB characters described with Σ values, they fundamentally originate from the atomic and electronic structure of GBs. To maximize beneficial effects of GBs in real polycrystalline materials, one therefore needs to fully understand the connection between the crystallographic characteristics, atomic structure and physical properties of GBs, through examining various GBs with respect to five degrees of freedom that describe GB crystallography.

To reveal their connection, atomistic simulations and first-principles calculations were extensively applied to symmetric tilt GBs (STGBs) in cubic crystal systems, including metal [11–14], covalent [15, 16] and ionic crystals [17–19]. In those studies, GB energies and structural units were systematically determined as functions of misorientation angle and rotational axis. Using low-energy structures, their electronic properties were also examined using density-functional theory (DFT) calculations. Furthermore, recent atomistic simulations indicated the existence of a vast number of metastable structures close in GB energy to the lowest energy structures, even for STGBs and twist GBs with low-Σ values [20–23]. However, proportions of STGBs are typically small in real polycrystals. In fact, previous experimental studies on GB distribution in polycrystals reported that except for $\Sigma 3$ twin GBs and STGBs with specific Σ values (e.g., $\Sigma = 9$ and 27), asymmetrical GBs were more frequently observed than STGBs [24–26]. So far it still remains an open question to what extent the atomic structure of STGBs is linked to that of general GBs, which are most likely to be asymmetrical with a wide spectrum of crystallographic characteristics.

For metals, some atomistic simulations focused on asymmetric tilt GBs (ATGBs) and indicated that ATGBs have nanofacet structures with more complex structural units than STGBs [27–34]. Tcshopp and McDowell systematically determined low-energy structures of ATGBs in Al and Cu [28, 29]. Their results indicated $\Sigma 3$, $\Sigma 5$ and $\Sigma 13$ ATGBs each ideally facet into STGB structural units with the same Σ values, whereas facet structures of $\Sigma 9$ and $\Sigma 11$ ATGBs contain structural units of $\Sigma 3(111)$ STGBs. Brown and Mishin also showed that $\Sigma 11$ ATGBs in Cu partially dissociate into nanofacets with non-$\Sigma 11$ and even non-coincident-site-lattice (CSL) structures [30], which cannot be interpreted with the CSL model alone. For a $\Sigma 5$ ATGB in bcc Fe, Medlin et al. showed that secondary GB dislocations are localized to facet junctions of $\Sigma 5$ structural units, suggesting that a density of GB dislocations is a dominant factor in nanofacet lengths [32]. Additionally, several theoretical works reported that shear deformation abilities along GB planes are much higher for ATGBs with non-planar interfaces than STGBs with planar interfaces [33, 34]. ATGBs and STGBs may thus be different in not only atomic structure but also GB properties, depending on their crystallography.

However, no systematic theoretical studies on ATGB in ionic crystals have been conducted in contrast to metals, although the atomic structure and energetics of STGBs have been widely investigated for oxide systems with simple crystal structures, e.g., MgO [17, 18], NiO [35, 36] and ZnO [37]. A few experiments examined atomic structures and GB properties of ATGBs in typical oxides, with a comparison to STGBs [38–42]. Bean et al. showed that in a MgO thin film, an incommensurate $(100)/(110)$ ATGB exhibits a flat interface composed of triangle structural units, by using STEM observations and first-principles calculations [42]. This ATGB also indicated 45% of reduction in band gap from its bulk value, while a band gap reduction at a $\Sigma 5$ STGB was $\sim$ 30%. This indicates that the atomic structure of the ATGB leads to the difference in electronic structure between the ATGB and STGB. Lee et al. reported that a $(430)/(001)$ ATGB in $SrTiO_3$ exhibited higher resistivity than $\Sigma 5$ STGBs [39]. The authors attributed the high resistivity to a high concentration of oxygen deficits at the faceted interface of the ATGB. However, it is currently unclear whether such differences between ATGBs and STGBs are significant in real ionic polycrystals, since the knowledge on the atomic structure of ATGBs is still very limited even for ionic systems with simple crystal structures.

This work aims to determine atomic structures, nanofacet structures and GB energies of ATGBs in MgO by using a simulated annealing (SA) method based on molecular dynamics (MD) simulations [18, 19]. Comparisons between ATGBs and STGBs are also made with respect to structural units and excess volume to investigate an origin of formation of ATGB atomic structures. The metastability of ATGBs is also examined by comparing the distribution of

metastable structures for ATGBs and STGBs. MgO is a typical ionic-bonding system, with the simple rock-salt structure. Analysis on MgO ATGBs will provide us fundamental insight into formation of nanofacet structures for ionic systems, which is expected to be applicable to ATGBs in other ionic systems. In addition, a comparison between ATGBs in MgO and fcc metals [29] is also made in order to reveal how the difference between their bonding states, namely ionic and metal bonding, affects preferential nanofacet structures for the two systems. The knowledge obtained from their comparison will shed the light to formation mechanisms of ionic and metal ATGB structures.

Method

Construction of ATGB

Table 1 lists crystallographic characteristics of ATGBs studied here. $\Sigma 5$ and $\Sigma 13$ ATGBs from low- to high-index boundary planes were examined, and their results were also compared to those of metal ATGBs in the literature [29]. As described in previous studies [28–30], the inclination angle Φ needs to be introduced to define the angle between the boundary planes of an ATGB and a reference STGB with the same Σ value. $\Sigma 5$ and $\Sigma 13$ ATGBs with the [001] tilt axis are defined between $0° < \Phi < 45°$. For $\Sigma 5$ ATGBs, $\Phi = 0°$ and $\Phi = 45°$ correspond to the $\Sigma 5(310)$ and $\Sigma 5(210)$ STGBs, respectively. For $\Sigma 13$ ATGBs, the reference STGBs are $\Sigma 13(510)$ at $\Phi = 0°$ and $\Sigma 13(320)$ at $\Phi = 45°$. The atomic structures of STGBs with the [001] tilt axis were also determined to compare structural units and GB energies of ATGBs and STGBs. Their crystallographic characteristics are contained in the Supporting Information.

A simulation cell of an ATGB is illustrated in Fig. 1a. Here, the z-axis is parallel to the [001] tilt axis. In order to satisfy periodic boundary conditions of the simulation cells for ATGBs, y-axis lengths of the adjacent grains have to match with each other. For this purpose, least common multiples of minimum y-axis lengths of the two grains were considered to construct the simulation cells. For example, a y-axis length of a $\Sigma 5(100)/(430)$ cell was obtained to extend a minimum y-axis length of the (001) grain by five times against a minimum y-axis length of the (430) grain.

Note that when an ATGB is modeled with three-dimensional (3D) periodic boundary conditions, the

Table 1 Information about crystallography and simulation cell for ATGBs. Φ represents the inclination angle. L_y is the y-axis length along the boundary plane

Σ	Boundary plane	Φ [deg.]	L_y [Å]
5	$(\bar{4}10)/(1980)$	4.40	86.83
	$(\bar{1}\bar{1}20)/(210)$	8.13	47.09
	$(\bar{8}10)/(740)$	11.31	33.96
	$(\bar{1}810)/(320)$	15.26	75.93
	$(100)/(430)$	18.44	21.06
	$(1210)/(980)$	23.20	50.72
	$(710)/(110)$	26.57	14.89
	$(920)/(670)$	30.96	38.83
	$(1130)/(790)$	33.69	24.01
	$(310)/(9130)$	36.87	33.30
	$(1970)/(11170)$	38.66	42.64
13	$(\bar{1}810)/(1760)$	8.13	75.93
	$(100)/(1250)$	11.31	54.75
	$(810)/(740)$	18.43	33.96
	$(1130)/(970)$	26.57	24.01
	$(1450)/(11100)$	30.96	62.61
	$(1770)/(110)$	33.69	38.72
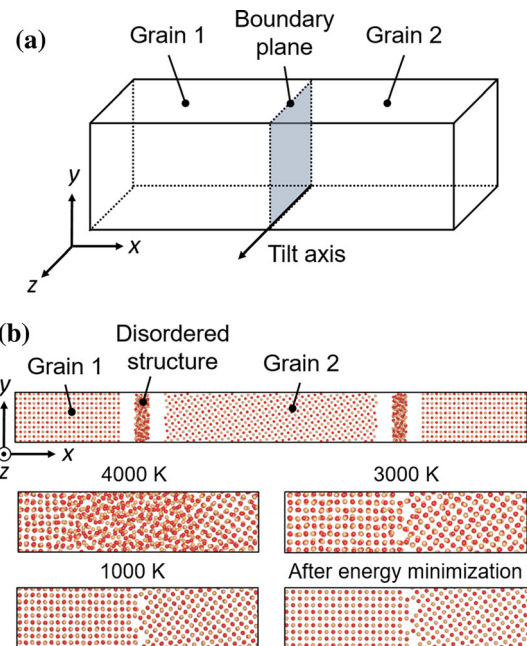
Figure 1 a Schematic illustration of a GB simulation cell. **b** Initial simulation cell for the SA method. The bottom pictures show snapshots at 4000 K, 3000 K and 1000 K during a SA simulation, and the structure after energy minimization.

simulation cell does not always satisfy rotational symmetry about the [001] axis with the center of rotation located at the center in the *x–y* plane, for an arbitrary translation of one grain to the other along the boundary plane. This often leads to distortion of a simulation cell in structural optimization. However, it is advantageous to use this type of simulation cell during SA simulation so as to prevent abrupt expansion of the GB region, as described in the next section. Thus a simulation cell with 3D periodic boundary conditions was first used in a SA simulation. Subsequently a simulation cell with the grains terminated at free surfaces was constructed from the simulation cell after the SA simulation, in order to calculate its GB energy.

Simulated annealing and γ-surface methods

Stable and metastable structures of the ATGBs were obtained using a SA method with MD simulations used in our previous studies [18, 19], as illustrated in Fig. 1b. Simulation cells for GBs are often constructed by cutting original perfect crystal structures according to the GB orientations in a straightforward manner. However, it is expected that ATGBs form nanofacets along the GB planes, where considerable atomic motions such as reconstruction and shuffling can take place. In order to facilitate such atomic motion in GB formation during simulations, thin layers of disordered atomic structures of MgO were initially introduced between the adjacent grains (see Fig. 1b). This disordered structure was created by performing an MD simulation at 8000 K for 20 ps, and subsequently, it was sandwiched between two grains.

The SA method was performed in the following procedures. Firstly, an MD simulation was performed at 4000 K for 30 ps. In this stage, the NVT condition was used to solidify the disordered structures and prevent large expansion of the simulation cell. The edge lengths were slightly increased by a few percent to relieve internal high pressure. Secondly, to equilibrate the edge lengths, MD simulations in the NPT condition were performed by decreasing temperature T from 3750 to 500 K in an increment of 250 K (3750 K $\leq T \leq$ 2500 K) and 500 K (2500 K $\leq T \leq$ 500 K). The holding time at each temperature was set at 30 ps. Finally, after running successive MD simulations at 500 K, 100 K and 50 K for 10 ps, the GB structures were optimized by

performing energy minimization. The Nosé–Hoover thermostat was used in the series of MD simulations. To obtain low-energy structures, the SA method mentioned was performed 20 and 50 times for each STGB and ATGB, respectively. For the ATGBs with the *y*-axis length larger than 50 Å, additional 50 SA simulations were performed, as it is expected that these ATGBs have a larger number of metastable structures and thus the lowest energy structures are more difficult to obtain than that of an ATGB with a shorter *y*-axis length.

Since two GBs in the individual simulation cells, which are introduced due to periodic boundary conditions, were independently relaxed in a SA simulation, their relaxed atomic structures were often different. Thus two simulation cells with either GB structures were created from one simulation cell after a SA simulation, by adding vacuum layers in the *x*-axis direction perpendicular to the GB planes and terminating the grains at free surfaces. The width of the vacuum layer was chosen to be 30 Å. The two simulation cells were again optimized using a conjugate gradient method in a constant volume condition, and finally their GB energy was calculated.

A γ-surface method was also used to confirm that a SA-based method is essential for obtaining low-energy nanofacet structures for ATGBs. In typical γ-surface methods, static energy minimization is employed to search for low-energy structures; however, the atomic positions are updated so that the total energy of a system always decreases at every iteration. Thus if significant atomic rearrangement, which often involves temporal increase in total energy, is required to obtain the global energy-minimum structure, such a structure cannot be obtained with the γ-surface method alone. In this method, different initial GB structures in atomic configuration at GBs were constructed, by shifting one grain relative to the other with a translational vector of 0.5 Å in the *y*- and *z*-axis directions along the boundary plane. All initial structures were relaxed by performing structural optimization.

Atomistic simulations were performed using the LAMMPS code [43]. A Buckingham-type interatomic potential was employed to calculate short-range interactions between ions, using a set of empirical parameters reported in the literature [44]. The rigid-ion model was used, and the formal charges of Mg and O ions were fixed to be + 2 and 2, respectively.

GB energy and excess volume of ATGBs

The GB energy of an ATGB, E_{GB}^{ATGB}, was calculated in two ways: one is to directly calculate E_{GB}^{ATGB} from an energy difference between the ATGB cell (E^{ATGB}) and the perfect-crystal cell ($E^{Perfect}$), by using the following equation:

$$E_{GB}^{ATGB} = \frac{E^{ATGB} - E^{Perfect}}{A} - E_1^{Surface} - E_2^{Surface} \qquad (1)$$

where A is an area of a macroscopic GB plane, and $E_1^{Surface}$ and $E_2^{Surface}$ are the surface energies of two surfaces at which two grains are terminated. The values of surface energies are listed in Supporting Information. Here, "macroscopic" means that A is calculated from the product of the y- and z-axis lengths, excluding an increase in GB area due to faceting. The other is to calculate E_{GB}^{ATGB} by assuming that an ATGB ideally facets into STGB structural units with the same Σ value. With this assumption, E_{GB}^{ATGB} as a function of Φ was calculated by using the following equation reported by Tcshopp and McDowell [28, 29]:

$$E_{GB}^{ATGB,TM} = E_{GB}^{STGB,1} \left\{ \cos \Phi - \sin \Phi \cdot \frac{\cos \alpha}{\sin \alpha} \right\} + E_{GB}^{STGB,2}$$
$$\cdot \frac{\sin \Phi}{\sin \alpha}$$
$$(2)$$

where $E_{GB}^{STGB,1}$ and $E_{GB}^{STGB,2}$ are the GB energies of two STGBs with the same misorientation of two grains (e.g., $\Sigma5(210)$ and $\Sigma5(310)$ for the $\Sigma5$ ATGBs), and α is the angle between the GB planes of the two STGBs. For the [001] system, α is 45°. If an ATGB ideally facets into STGB structural units and also its facet junctions do not involve large distortion of the structural units, E_{GB}^{ATGB} obtained from Eqs. (1) and (2) should be the same. On the other hand, if the ATGB contains STGB structural units with different Σ values or its facet junctions lead to an energy penalty, E_{GB}^{ATGB} obtained from Eq. (1) should deviate from that of Eq. (2). The ideal value of excess volume per unit area of a GB plane, V_{GB}, was also defined in the same manner:

$$V_{GB} = V_{GB}^{STGB,1} \left\{ \cos \Phi - \sin \Phi \cdot \frac{\cos \alpha}{\sin \alpha} \right\} + V_{GB}^{STGB,2} \cdot \frac{\sin \Phi}{\sin \alpha}$$
$$(3)$$

where $V_{GB}^{STGB,1}$ and $V_{GB}^{STGB,2}$ are the excess volume of the STGB counterparts.

Results and discussion

Grain boundary energy and structural unit of STGB

It is prerequisite to examine structural properties and energetics of STGBs, in order to understand those of ATGBs. Figure 2 shows the lowest energy structures of the $\Sigma5$, $\Sigma13$ and $\Sigma17$ STGBs in order of misorientation angle 2θ. From $\Sigma13(510)$ to $\Sigma17(530)$, their GB cores have empty spaces, whereas $\Sigma13(320)$ contains ions located on the boundary plane without an empty space. These "open" and "dense" structures are also obtained from density-functional theory (DFT) calculations [45] (see also the Supporting Information). Note that for $\Sigma13(320)$, DFT calculations show two stable structures whose GB energies are very close with a difference of 4×10^{-3} J/m^2. The empirical potential also predicts one of the two structures as the stable structure, and thus, its transferability is reasonably maintained for all STGBs studied.

Here the $\Sigma17(410)$ and $\Sigma17(530)$ STGBs are also shown, as their structural units are contained in $\Sigma5$ and $\Sigma13$ ATGBs as discussed later. $\Sigma17(410)$ has an open structure similar to those of $\Sigma13(510)$ and $\Sigma5(310)$, with a difference in the number of atoms consisting of their structural units. The sizes of the structure units tend to decrease with increasing 2θ value. In contrast, $\Sigma17(530)$ has two different structure units. The one is the same with that of $\Sigma5(210)$ as indicated by the green line, while the other is a six-membered ring (black line) that is not contained in the $\Sigma13(320)$ STGB.

Figure 3a shows GB energies of STGBs (E_{GB}^{STGB}) as a function of 2θ. There are two cusps for $\Sigma5(210)$ and for $\Sigma5(310)$, at which E_{GB}^{STGB} is 1.78 J/m^2 and 1.96 J/m^2, respectively. The maximum value of E_{GB}^{STGB} is 2.19 J/m^2 for $\Sigma17(530)$. These trends are in agreement with DFT results (Supporting Information), although E_{GB}^{STGB} calculated from the empirical potential were 0.26–0.39 J/m^2 larger than E_{GB}^{STGB} calculated from DFT calculations for the six STGBs in Fig. 2. It is noted that E_{GB}^{STGB} obtained from the SA and γ-surface methods are identical, with just small differences for $\Sigma97(940)$ and $\Sigma65(530)$. For STGBs, the two methods thus can provide similar low-energy structures. Figure 3b shows excess volume V_{GB} as a function of 2θ. V_{GB} also reflects the difference between open and dense structures: from $\Sigma13(510)$ to $\Sigma17(530)$, V_{GB} ranges

Figure 2 Structural units viewed along the [001] tilt axis for Σ5, Σ13 and Σ17 STGBs in order of misorientation angle 2θ. They are the lowest energy structures obtained from the SA method. The light- and dark-gray balls represent Mg and O ions, respectively.
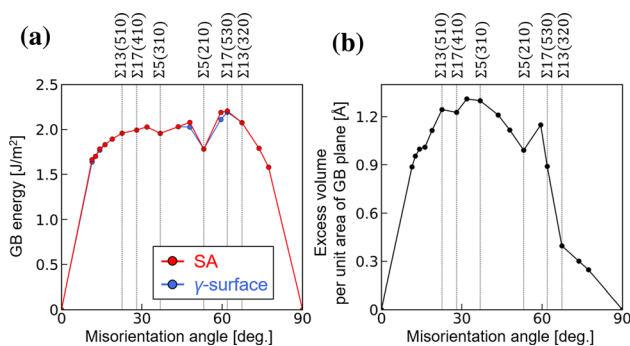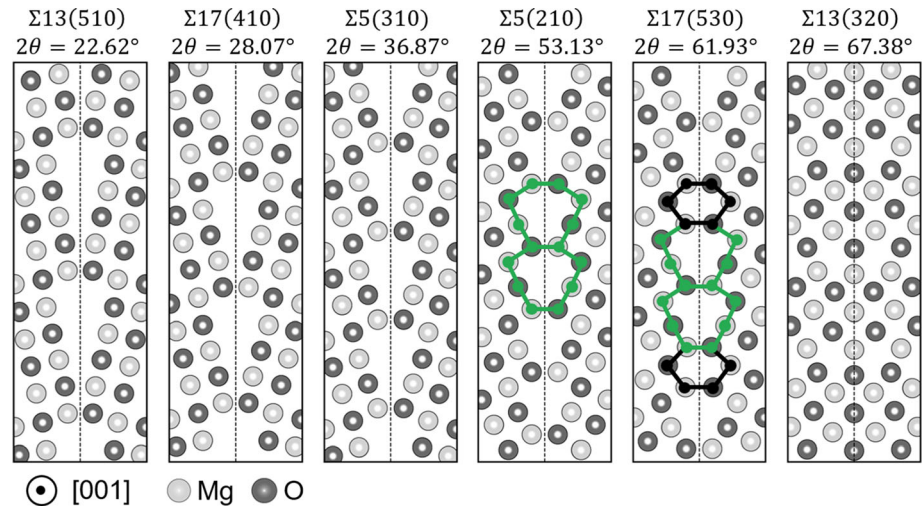
Figure 3 **a** GB energy and **b** excess volume per unit area of a GB plane as a function of misorientation angle 2θ for STGBs with the [001] tilt axis. The GB energies are calculated from the SA method (red line) and the γ-surface method (blue line).

similar values, whereas it sharply decreases for Σ13(320). Thus if a GB structure consists of only an open or a dense structure, V_{GB} is predominantly determined by 2θ.

Grain boundary energy of ATGB

Figure 4 shows E_{GB}^{ATGB} as a function of inclination angle Φ. The ideal values (black line, $E_{GB}^{ATGB,TM}$) are obtained from Eq. (2), and the calculated values (red line, $E_{GB}^{ATGB,SA}$) are computed using the energy-minimum structures obtained for the SA method (red line). The calculated results using the γ-surface method with static energy minimization (blue line, $E_{GB}^{ATGB,\gamma}$) are also plotted. As shown in Fig. 4a, most of the Σ5 ATGBs have $E_{GB}^{ATGB,SA}$ similar to $E_{GB}^{ATGB,TM}$, although $E_{GB}^{ATGB,SA}$ is slightly higher than $E_{GB}^{ATGB,TM}$ with differences between 0.03 and 0.05 J/m².

However, the particular high-index ATGBs have $E_{GB}^{ATGB,SA}$ values larger than $E_{GB}^{ATGB,TM}$, with differences between 0.16 and 0.21 J/m².

For the Σ13 ATGBs (Fig. 4b), $E_{GB}^{ATGB,SA}$ values do not simply follow $E_{GB}^{ATGB,TM}$ and are more complicated than those of the Σ5 ATGBs. At $\Phi = 8.13°$ and 30.96°, $E_{GB}^{ATGB,SA}$ larger than $E_{GB}^{ATGB,TM}$, whereas $E_{GB}^{ATGB,SA}$ is smaller than $E_{GB}^{ATGB,TM}$ at $\Phi = 11.31°$, 18.43° and 26.57°. At $\Phi = 33.69°$, $E_{GB}^{ATGB,SA}$ and $E_{GB}^{ATGB,TM}$ have close values with the difference of less than 0.02 J/m². Even for this ATGB, the nanofacet does not consist of purely Σ13 STGB structural units, as mentioned in the next section. These results demonstrate that
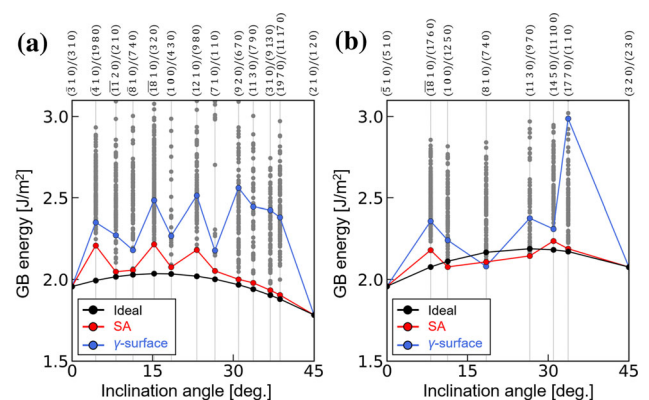
Figure 4 GB energies calculated from Eq. (2) (black line), SA-simulation results (red line) and γ-surface results (blue line) for **a** Σ5 and **b** Σ13 ATGBs. The metastable structures obtained from the SA method are represented by the gray circles distributed vertically at each Φ. Each circle corresponds to one metastable structure.

whether calculated E_{GB}^{ATGB} follows its ideal value greatly depends on the inclination angle and Σ value.

The above trends in GB energy in MgO are in contrast to $\Sigma5$ and $\Sigma13$ ATGBs in Cu and Al reported by Tschopp and McDowell [29]. For their calculations of $\Sigma5$ ATGBs, the calculated and ideal E_{GB}^{ATGB} were nearly the same in the whole Φ value, including high-index ATGBs such as $(\overline{4}10)/(1980)$, $(\overline{18}10)/(320)$ and $(1210)/(980)$ ATGBs. For $\Sigma13$ ATGBs in the fcc metals [29], the calculated E_{GB}^{ATGB} was reported to also well follow the ideal E_{GB}^{ATGB}, with small differences of ~ 0.02 J/m^2. This comparison suggests that even for the low-Σ ATGBs, there may be large differences in energetics of ATGBs between MgO and the fcc metals. This difference is highly likely to arise from the difference in low-energy structural unit, which are originally determined by bonding state, between ionic and metal systems.

It is worthwhile to compare E_{GB}^{ATGB} obtained from the SA and γ-surface methods (red and blue line, respectively). For $\Sigma5$ ATGBs, $E_{GB}^{ATGB,\gamma}$ is entirely larger than $E_{GB}^{ATGB,SA}$ with differences ranging from 0.12 J/m^2 to 0.56 J/m^2. This is also the case of the low-index ATGBs, i.e., the $(100)/(430)$ and $(710)/(110)$ ATGBs. A similar trend is also observed for the $\Sigma13$ system; the $(1770)/(110)$ ATGB especially shows a large difference between $E_{GB}^{ATGB,SA}$ and $E_{GB}^{ATGB,\gamma}$, with as large as 0.80 J/m^2. These differences arise from differences between low-energy atomic structures obtained from the SA and γ-surface methods, as will be shown later. These results clearly indicate that the γ-surface method is unable to explore low-energy ATGB structures obtained from the SA method.

It is also noted that there exist many metastable structures obtained from the SA method, as represented by the gray circles distributed vertically at each Φ. The metastable structures were obtained from structural optimization at 0 K. Here a metastable structure was defined as a local minimum structure different in atomic configuration from the most stable one at 0 K. It is noted that in this definition, the stability of a GB is based on zero-temperature potential energy and volume, and thus a metastable structure at 0 K is not exactly the same as its equilibrium structure at finite temperature.

All ATGBs studied have at least one metastable structure close in E_{GB}^{ATGB} to the lowest energy structure, with their GB-energy differences of less than 0.1 J/m^2. In addition, there are multiple near-lowest structures for each ATGB. Therefore not only the lowest energy structure but also metastable structures may be also essential for understanding the atomic structure of actual ATGBs in polycrystals. A detail analysis will be carried out in the section of metastability of ATGB.

Atomic structure of ATGB

Figures 5 and 6 show nanofacets of $\Sigma5$ ATGBs. For the ATGBs whose E_{GB}^{ATGB} is close to the ideal value (Fig. 4a), their nanofacets consist of only $\Sigma5(210)$ and $\Sigma5(310)$ STGBs as represented by the green and blue lines. For these ATGBs, the ratio of the $\Sigma5(310)$ to $\Sigma5(210)$ structural units decreases with increasing Φ (see Table 2), while keeping their shapes. These changes in the ratio can be understood from the crystallographic prediction. As indicated by the dashed lines in the panel of the $(100)/(430)$ ATGB, the angle between the $\Sigma5(210)$ and $\Sigma5(310)$ segments is maintained to be 45°, which is observed for all ATGBs in Fig. 5.

In comparing between the current result of MgO and the previous result of Cu [29], the same trend is that nanofacets in these two systems dissociate into purely the lowest energy structural units of $\Sigma5(210)$ and $\Sigma5(310)$ STGBs, without other structural units. A large difference is the width of nanofacets perpendicular to the boundary plane. For MgO, the nanofacets are formed across two grains, involving a significant reconstruction of atomic arrangements that originally have the perfect crystal structure. As a result, these nanofacets have saw-toothed structures. For Cu ATGBs [29], on the other hand, changes in atomic arrangement are confined to only the GB core region, with a few Å in width. Another difference is that for MgO ATGBs, structural units appear to be more distorted than those for Cu ATGBs, particularly at the facet junction where $\Sigma5(210)$ and $\Sigma5(310)$ structural units are adjacent to each other. Their distortion probably results in the calculated E_{GB}^{ATGB} slightly higher than the ideal value (Fig. 4a).

For the $\Sigma5$ ATGBs whose E_{GB}^{ATGB} deviates from the ideal value (Fig. 6), two types of non-$\Sigma5$ structural units are contained. One is the $\Sigma17(410)$ STGBs as represented by the red line. The other is similar to the structural unit of an incommensurate $\{100\}/\{110\}$ ATGB (black line), as observed by Bean et al. [39]. The

Figure 5 Nanofacets of Σ5 ATGBs whose E_{GB}^{ATGB} are similar to the ideal values (Fig. 4a) in order of inclination angle Φ. These structures are obtained from the SA method. The green and blue lines represent the structural units of Σ5(210) and Σ5(310) STGBs, respectively.
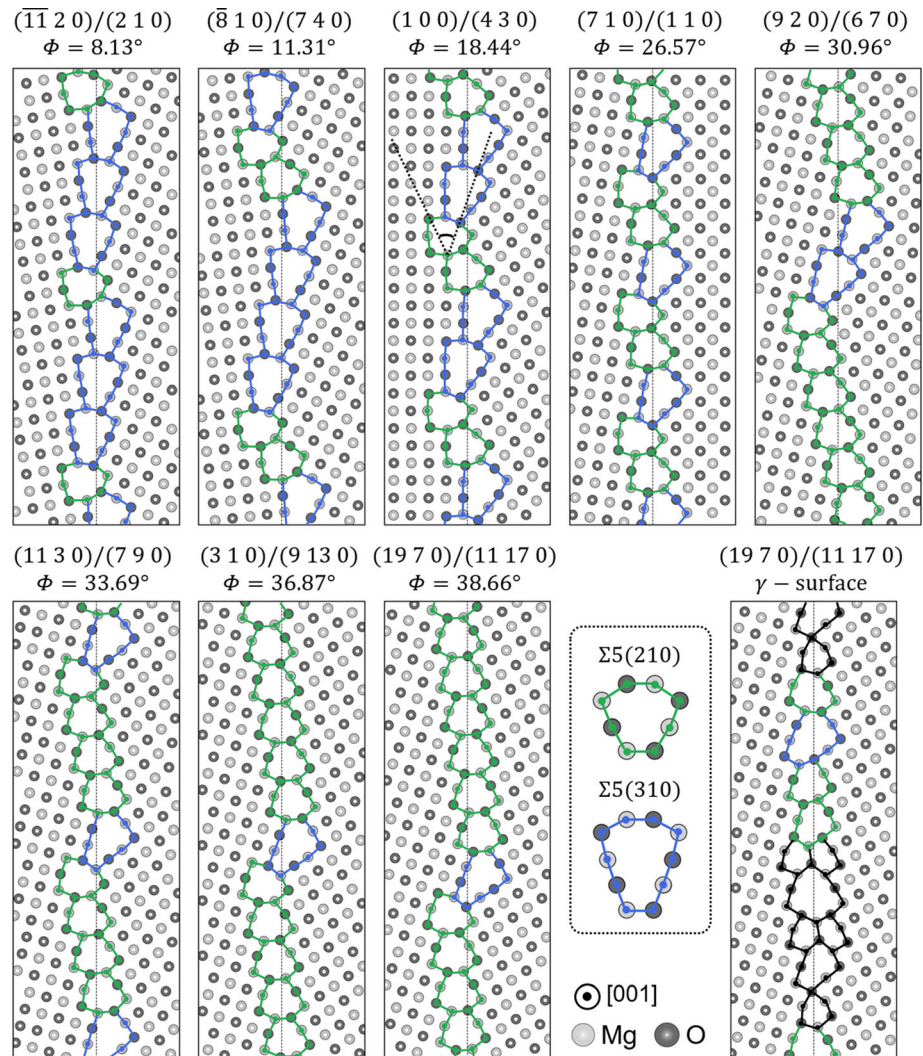
(410)/(1980) and (1210)/(980) ATGBs contain both the structural units, whereas the $\left(\overline{18}\,10\right)/(320)$ ATGB contains only {100}/{110} ATGBs. Even for metastable structures obtained from the SA method, nanofacets composed of only Σ5(210) and Σ5(310) STGBs are absent. There are mainly two possible reasons that a pure Σ5 nanofacet was not observed. One is that such a nanofacet is not necessarily the lowest energy structure for the three high-index ATGBs, possibly due to a high energy penalty at the facet junction at Σ5 STGBs. The other is that the pure Σ5 nanofacets are also the lowest energy ones for the three ATGBs, but their probability of being formed is low because of the existence of a vast number of metastable structures, as discussed in the next section. Although it is still unclear whether these structures are the global minimum, this result suggests

that the presence of Σ17(410) STGBs and {100}/{110} ATGBs does not lead to a large increase in E_{GB}^{ATGB} for Σ5 ATGBs.

It is noted that there is a clear difference between the lowest energy structures obtained from the SA and γ-surface methods, as indicated in the bottom panels for the (1970)/(11170) ATGB in Fig. 5. The SA nanofacet is composed of only Σ5(210) and Σ5(310) STGBs, involving reconstruction of atomic arrangements in the lattice region. The γ-surface nanofacet contains non-Σ5 structures (black line) and lies parallel to the boundary plane. This nanofacet is energetically much higher than the SA nanofacet as previously shown in Fig. 4a.

For Σ13 ATGBs (Fig. 7), their nanofacets are more complex than the Σ5 ATGBs in the sense that no facets consist of purely Σ13(510) and Σ13(320) STGBs, and different Σ structural units are always present.
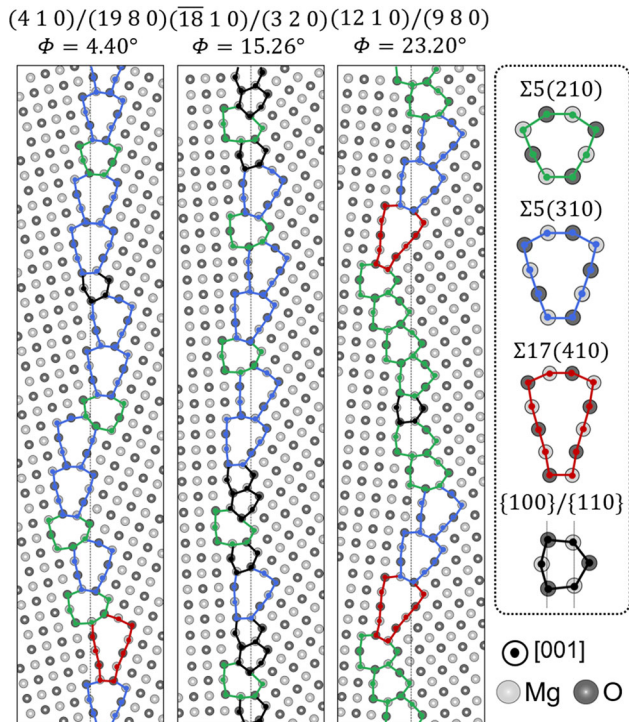
Figure 6 Nanofacets of the Σ5 ATGBs whose E_{GB}^{ATGB} deviate from the ideal values (Fig. 4a). These structures are obtained from the SA method. The green, blue and red lines represent the Σ5(210), Σ5(310) and Σ17(410) STGB structural units, respectively. The black one appears to be the structural unit of an incommensurate {100}/{110} ATGB.

Table 2 Ratio of Σ5(210) to Σ5(310) structural units in one period along the y-axis for Σ5 ATGBs. The values in the bracket parentheses are the ideal value predicted from crystallography.

Boundary plane	Ratio of structural units	
	Σ5(310)	Σ5(210)
$(\bar{4}10)/(1980)$	9 (6)	4 (1)
$(\bar{1}\bar{1}20)/(210)$	3 (3)	1 (1)
$(\bar{8}10)/(740)$	2 (2)	1 (1)
$(\bar{1}810)/(320)$	3 (4)	2 (3)
$(100)/(430)$	1 (1)	1 (1)
$(1210)/(980)$	1 (2)	2 (3)
$(710)/(110)$	1 (1)	2 (2)
$(920)/(670)$	1 (1)	3 (3)
$(1130)/(790)$	1 (1)	4 (4)
$(310)/(9130)$	1 (1)	6 (6)
$(1970)/(11170)$	1 (1)	8 (8)

This tendency is especially significant for the (810)/(740) and (1130)/(970) ATGBs. The (810)/(740)
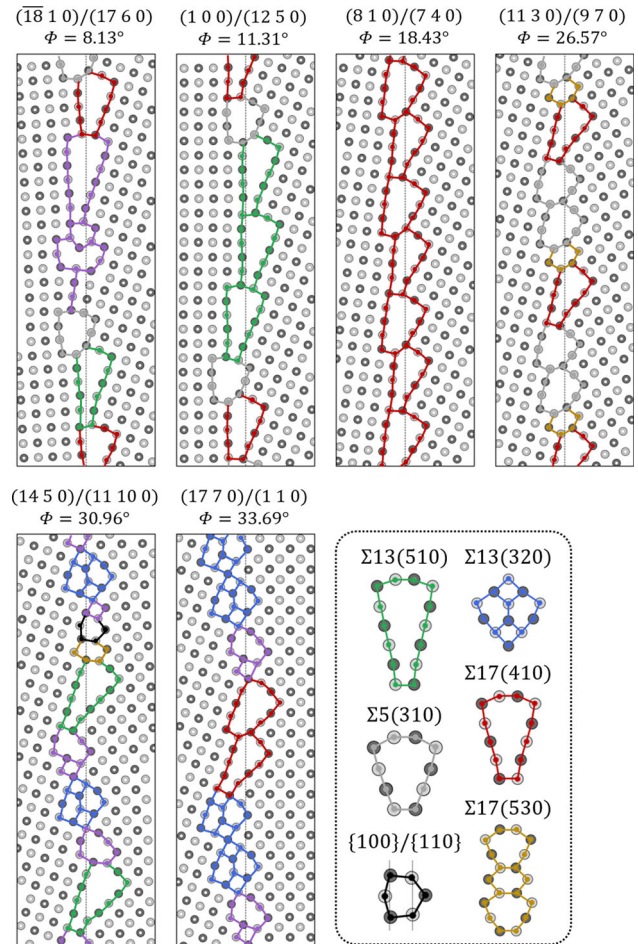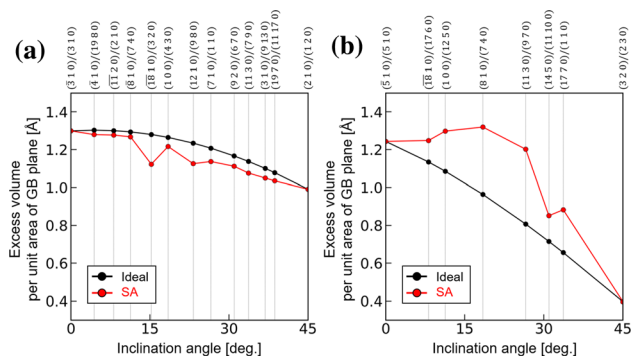

Figure 7 Nanofacets obtained from the SA method for the Σ13 ATGBs. The green and blue lines represent the Σ13(510) and Σ13(320) structural units, respectively. The gray, red and yellow ones correspond to the Σ5(310), Σ17(410) and Σ17(530) structural units, respectively. The purple lines indicate the structures that cannot be classified into any low-Σ STGBs.

ATGB consists of only Σ17(410) STGB structural units, although their shapes are distorted from the original one. The (1130)/(970) ATGB also does not contain Σ13 STGB structural units, but it consists of a series of non-Σ13 STGBs: Σ17(410), Σ5(310) and a part of Σ17(530). The other Σ13 ATGBs also contain non-Σ13 structural units, including segments that do not belong to at least low-Σ STGBs, as indicated by the purple lines. These results suggest that Σ13 ATGBs in MgO are likely to have atomic structures different from a simple combination of Σ13(510) and Σ13(320) STGBs.

The great deviation in structural unit type for the Σ13 ATGBs is probably due to a large difference between V_{GB} of the Σ13(510) and Σ13(320) STGBs,

which is as large as 0.85 Å (see Fig. 3b). This difference also influences V_{GB} of the Σ13 ATGBs, as shown in Fig. 8. For Σ5 ATGBs in Fig. 8a, V_{GB} monotonically decreases with Φ and qualitatively follows the ideal value. For Σ13 ATGBs in Fig. 8b, on the other hand, the calculated V_{GB} keeps 1.20–1.32 Å in the range of Φ = 0° and 26.57°, while its ideal V_{GB} almost linearly decreases. In this range of Φ, V_{GB} has similar values because the nanofacets do not contain dense structures (i.e., the Σ13(320) STGB) but basically consist of open structures, as shown in Fig. 7. At Φ = 30.96°, V_{GB} abruptly decreases to 0.85 Å and subsequently decreases with increasing Φ. In this range the ATGBs partly contain Σ13(320) STGBs, which have smaller V_{GB}, as indicated by the blue lines in the bottom panels in Fig. 7.

The above trend of the Σ13 ATGB structures in MgO is very different from those in Cu in the literature [29]. In Cu, the Σ13 ATGBs studied were reported to dissociate into Σ13(510) and Σ13(320) STGBs without other Σ-value STGBs. These Σ13 STGB structural units have similar shapes with "dense" structures in the context of MgO GBs, as shown in the previous study. As a result, their excess volumes probably also have similar values. It is thus likely that they can coexist adjacent to each other in one Σ13 ATGB, without a large energy increase. On the other hand, MgO STGBs have both dense and open structures (Fig. 2). This difference between the MgO and metal structural units presumably arises from the difference between their bonding states. For MgO, Mg and O ions are always adjacent even at GBs, while mostly maintaining the atomic arrangement of its perfect crystal. This trend is clearly due to
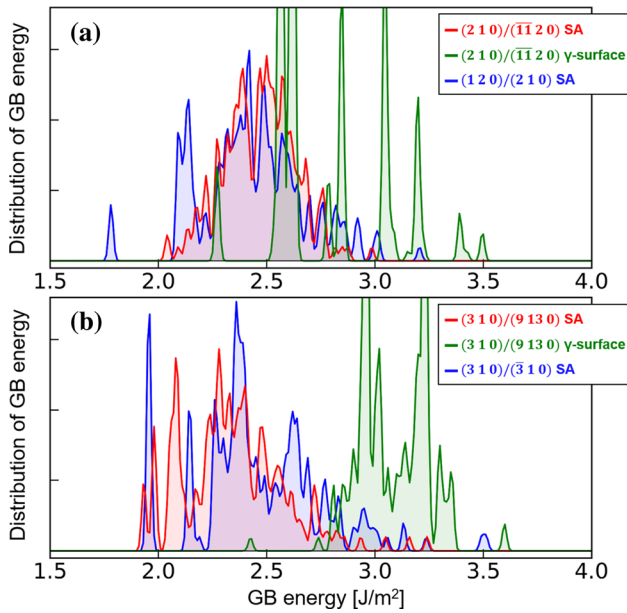
the fact that the Coulomb interaction of Mg and O ions is also a critical effect in determining the shape of a structural unit. Due to this effect, the preferential atomic configuration of Mg and O ions at a GB is likely to be more restrictive than that of metal atoms, leading to the existence of dense and open structures depending on misorientation angle. However, if the two structures belong to the same Σ system as is observed for Σ13(320) and Σ13(510), their coexistence is most likely to result in a large energy penalty due to significant distortion of their structural units, as shown in Fig. 8b. For other ionic systems, ATGBs with particular Σ values may also show a trend similar to Σ13 ATGBs in MgO, that is, their nanofacets do not simply consist of the same Σ STGBs due to a large difference between the excess volumes of STGB counterparts.

The above comparison between the atomic structures of the Σ5 and Σ13 highlights that whether ATGBs dissociate into STGBs with the same Σ value greatly depends on their GB characters. If an ATGB contains different Σ structural units, GB properties also may be changed from a simple combination of its STGBs counterparts.

Metastability of ATGB

Recent molecular simulation studies have indicated that there possibly exist many metastable structures close in ΔE_{GB} to the lowest energy structures, even for STGBs with low-Σ values [20–23]. Here we examine metastable structures of ATGBs, by comparing STGBs. Figure 9 shows the distribution of ΔE_{GB} for four GBs. In the y-axis direction, five repeats of the $(120)/(210)$ and $(310)/(\overline{3}10)$ STGB cells are the same in length and thereby in GB area as one repeat of the $(210)/(\overline{11}20)$ and $(310)/(9130)$ ATGB cells, respectively. Thus one can directly compare the distribution of GB energies of the ATGBs and STGBs, by excluding the effect of the difference in GB area. Totally 100 SA simulations were performed, and 200 structures were used to obtain the distribution for each GB.

In Fig. 9a, the SA-based distribution of ΔE_{GB}^{STGB} for the $(120)/(210)$ STGB (blue line) shows the peak of the lowest energy structure at 1.78 J/m^2 and the peaks of metastable structures at about 2.09–2.14 J/m^2. The peaks of the lowest energy and metastable structures are thus clearly separated. By contrast, the SA-based distribution of ΔE_{GB}^{ATGB} for the

Figure 8 Excess volume V_{GB} obtained from the ideal value (black line) and the SA method (red line) as a function of inclination angle Φ: **a** Σ5 and **b** Σ13 ATGBs. The lowest energy structures are used to calculate V_{GB}.

Figure 9 Distribution of GB energies for $\Sigma 5$ ATGBs and STGBs: **a** the $(210)/(\overline{11}20)$ ATGB and the $\Sigma 5(2\ 1\ 0)$ STGB, and **b** the $(310)/(9130)$ ATGB and the $\Sigma 5(3\ 1\ 0)$ STGB. The red and green lines represent the distribution obtained from the SA and γ-surface methods, respectively, for the ATGBs. A Gaussian function with a standard deviation of 0.01 is used to draw the GB-energy distribution as a continuous value.

$(210)/\left(\overline{11}20\right)$ ATGB (red line) shows that the peaks of the lowest energy and metastable structures are very close without a clear separation. The ΔE_{GB}^{ATGB} values of the other metastable structures are also continuously distributed from that of the lowest energy structure. These results indicate that the $(210)/(\overline{11}20)$ ATGB has more metastable structures close in ΔE_{GB}^{ATGB} to the lowest energy structure than the $(120)/(210)$ STGB. As a result of the presence of many metastable structures, the probability of forming the lowest energy structure becomes low.
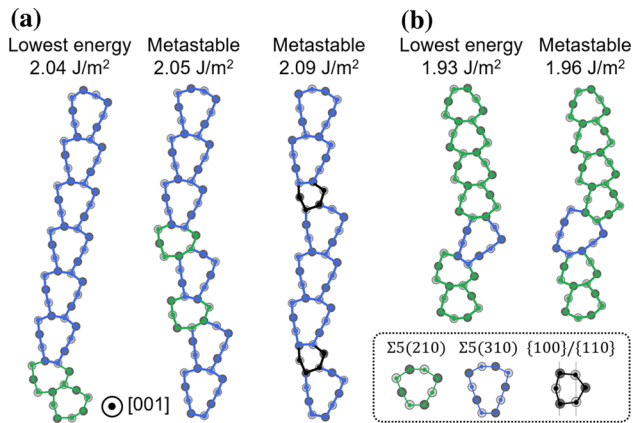
A similar difference is also observed for the $(310)/\left(\overline{3}10\right)$ STGB and the $(310)/(9130)$ ATGB, as shown in Fig. 9b, although the overall distribution is distinct from that of the $(210)/\left(\overline{11}20\right)$ ATGB. For the $(310)/\left(\overline{3}10\right)$ STGB, there is a peak corresponding to the lowest energy structure at 1.96 J/m². A peak arising from a metastable structure is also clearly observed at 2.14 J/m², for which E_{GB}^{STGB} is 0.18 J/m² larger than the lowest E_{GB}^{STGB}. At higher values than the two peaks, E_{GB}^{STGB} is continuously distributed. For

the $(310)/(9130)$ ATGB, there are two peaks close to each other at 1.93 J/m² and 1.98 J/m², which correspond to the lowest energy and metastable GBs obtained from the SA method. At higher-energy region, E_{GB}^{ATGB} is broadly distributed without a clear separation of each peak. The $(310)/(9130)$ ATGB is thus also likely to have a higher probability of forming metastable structures than the lowest energy structure.

It is noted that the distributions obtained from the SA and γ-surface methods are different in peak position and its magnitude, as indicated in Fig. 9. In static calculations, an optimized structure typically depends on its initial structure, particularly when there exist multiple metastable structures. Due to this fact, the γ-surface distribution shows strong peaks for both the ATGBs, which are entirely located at higher values of E_{GB}^{ATGB} than the SA distribution. This indicates that for the ATGBs, static calculations sample only particular metastable structures with high E_{GB}^{ATGB}. Thus the SA method is indeed likely to be a better choice for exploring the low-energy atomic structures of ATGBs.

To show how metastable structures of ATGBs are generated, three typical examples observed are visualized in Fig. 10. To explore metastable structures close in GB energy to the most stable ones, GB structures obtained from SA simulations and subsequent structural optimizations were sorted by the lower GB energies. Then, if differences between GB energies were larger than around 10^3 J/m², their structural units and configuration were checked manually. The first is that the ratio of two STGB structural units is the same between the lowest energy and metastable structures, but the order of their arrangements along the y-axis is different. As shown in Fig. 10a, the lowest energy structure has two $\Sigma 5(210)$ structural units adjacent to each other, whereas a metastable structure (the center picture in Fig. 10a) has those separated by one $\Sigma 5(310)$ structural unit. The difference leads to a just slight increase of E_{GB}^{ATGB} by 0.01 J/m². This type of metastable structure is also observed for other $\Sigma 5$ ATGBs studied, e.g., the $(100)/(430)$ and $\left(\overline{8}10\right)/(740)$ ATGBs. The second is that non-$\Sigma 5$ and non-$\Sigma 13$ structural units are formed, as illustrated in the right picture in Fig. 10a. In this case, two incommensurate {001}/ {110} units are formed, without formation of $\Sigma 5(210)$

(a)

Lowest energy 2.04 J/m²   Metastable 2.05 J/m²   Metastable 2.09 J/m²

(b)

Lowest energy 1.93 J/m²   Metastable 1.96 J/m²

⊙ [001]

Σ5(210)   Σ5(310)   {100}/{110}

Figure 10 Arrangement of structural units in one period viewed along the [001] tilt axis. **a** the $(\overline{1}120)/(210)$ ATGB and **b** the $(310)/(9130)$ ATGB. The green, blue and black lines represent structural units of Σ5(210), Σ5(310) and {100}/{110}.

units. The increase in E_{GB}^{ATGB} is as small as 0.05 J/m² despite the fact that constituent structural units are different. The third is that different facet junctions are formed by connecting structural units differently in space, while keeping the order of their arrangements along the y-axis, as illustrated in Fig. 10b. In this case, a Σ5(310) structural unit is located at the facet junction in both the lowest energy and metastable structures, but ions belonging to both Σ5(310) and Σ5(210) are different. This difference merely leads to an increase of E_{GB}^{ATGB} by 0.03 J/m². As another metastable structure, structural vacancies are also often introduced, although this type is not illustrated here. In this case, some atomic columns of structural units have lower atomic density than the lattice region.

With a combination of these metastable structures mentioned, a wide spectrum of metastable structures can be generated, although some structures would have high E_{GB}^{ATGB}. It is thus likely that their configurational entropy is large, and as a result the probability of forming the lowest energy structure becomes lower than that of metastable structures. Recent atomistic simulations for STGBs and twist GBs [20–23] varied atomic densities at GB regions by systematically removing/adding GB atoms and demonstrated that the atomic densities are also essential for exploring low-energy structures. Although our SA method also partly takes this factor in account as structural vacancies are spontaneously introduced, a systematic examination was not conducted. To fully understand ATGB metastability, atomic densities at

GB may be also important, in addition to those shown in Fig. 10.

The results of the ATGB metastability indicate that even Σ5 ATGBs with low-index boundary planes have a large number of metastable structures, some of which are close in GB energy to the lowest energy structure. In real polycrystals, it is expected that general GBs have more complex nanofacet structures with high-index boundary planes and thus a larger number of low-energy metastable structures than the Σ5 ATGBs in Fig. 9. As a result, metastable structures may be more frequently observed than the lowest energy structures, resulting in a more dominant influence on GB distribution and thereby polycrystalline microstructure.

Conclusions

The atomic structure of asymmetric tilt grain boundaries (ATGBs) in MgO has been explored by performing a simulated annealing (SA) method with molecular dynamics, in comparison with a γ-surface method. Σ5 and Σ13 ATGBs from low- to high-index planes were examined. The lowest energy structures obtained from the SA method are clearly lower than those of the γ-surface method, demonstrating the importance of SA methods for searching for low-energy structures. For Σ5 ATGBs, their nanofacets consist of purely the structural units of Σ5(210) and Σ5(310) symmetric tilt grain boundaries (STGBs). However, particular Σ5 ATGBs partly contain non-Σ5 structural units, leading to increase in GB energy from their ideal values. For the Σ13 ATGBs studied, nanofacets do not consist of only Σ13(320) and Σ13(510) STGBs, but always contain non-Σ13 structural units even for low-index ATGBs. This is probably due to that fact that the difference in excess volume between the two STGBs is large, and thus their coexistence leads to large increase in GB energy. Furthermore, analyses of ATGB metastability indicate that there exist a various types of metastable structures, involving variation in structural unit, its arrangement and facet junction. Due to their variation, configuration entropies of metastable structures become large, and as a result, the lowest energy structures have low probabilities of being formed.

Acknowledgements

Compliance with ethical standards

Conflict of interest The authors declare that they have no conflict of interest.

Electronic supplementary material: The online version of this article (https://doi.org/10.1007/s10853-020-05488-4) contains supplementary material, which is available to authorized users.

References

[1] Lin P, Palumbo G, Erb U, Aust KT (1995) Influence of grain boundary character distribution on sensitization and inter-granular corrosion of alloy 600. Scr Metall Mater 33:1387–1392

[2] Watanabe T, Tsurekawa S (1999) The control of brittleness and development of desirable mechanical properties in polycrystalline systems by grain boundary engineering. Acta Mater 47:4171–4185

[3] Jones R, Randle V (2010) Sensitisation behavior of grain boundary engineered austenitic stainless steel. Mater Sci Eng A 527:4275–4280

[4] Hu C, Xia S, Li H, Liu T, Zhou B, Chen W, Wang N (2011) Improving the intergranular corrosion resistance of 304 stainless steel by grain boundary network control. Corros Sci 53:1880–1886

[5] XiaHL ST, Zhou BX (2011) Applying grain boundary engineering to Alloy 690 tube for enhancing intergranular corrosion resistance. J Nucl Mater 416:303–310

[6] Sato Y, Yamamoto T, Ikuhara Y (2007) Atomic structures and electrical properties of ZnO grain boundaries. J Am Ceram Soc 90:337–357

[7] Li XM, Chou YT (1996) High angle grain boundary diffusion of chromium in niobium bicrystals. Acta Mater 44:3535–3541

[8] Nakagawa T, Nishimura H, Sakaguchi I, Shibata N, Matsunaga K, Yamamoto T, Ikuhara Y (2011) Grain boundary character dependence of oxygen grain boundary diffusion in α-Al_2O_3 bicrystals. Scripta Mater 65:544–547

[9] Tai K, Lawrence A, Harmer MP, Dillon SJ (2013) Misorientation dependence of Al_2O_3 grain boundary thermal resistance. Appl Phys Lett 102:034101

[10] Lee D, Lee S, An BS, Kim TH, Yang CW, Suk JW, Baik S (2017) Dependence of the in-plane thermal conductivity of graphene on grain misorientation. Chem Mater 29:10409–10417

[11] Wolf D (1989) Structure-energy correlation for grain boundaries in f.c.c. metals-II. Boundaries on the (110) and (113) planes. Acta Metall Mater 10:2823–2833

[12] Wolf D (1990a) Structure-energy correlation for grain boundaries in f.c.c. metals-III. Symmetrical tilt boundaries Acta Metall Mater 38:781–790

[13] Rittner JD, Seidman DN (1996) <110> symmetric tilt grain-boundary structures in fcc metals with low stacking-fault energies. Phys Rev B 54:6999–7015

[14] Hahn EN, Fensin SJ, Germann TC, Meyers MA (2016) Symmetric tilt boundaries in body-centered cubic tantalum. Scripta Mater 116:108–111

[15] Kohyama M (2002) Computational studies of grain boundaries in covalent materials. Model Simul Mater Sci Eng 10:R31–R59

[16] Wang L, Yu W, Shen S (2018) Revisiting the structures and energies of silicon <110> symmetric tilt grain boundaries. J Mater Res 34:1021–1033

[17] Harding JH, Harris DJ (1999) Computer simulation of general grain boundaries in rocksalt oxides. Phys Rev B 60:2740–2746

[18] Yokoi T, Yoshiya M (2018) Atomistic simulations of grain boundary transformation under high pressures in MgO. Phys B 532:2–8

[19] Fujii S, Yokoi T, Yoshiya M (2019) Atomistic mechanisms of thermal transport across symmetric tilt grain boundaries in MgO. Acta Mater 171:154–162

[20] Han J, Vitek V, Srolovitz DJ (2016) Grain-boundary metastability and its statistical properties. Acta Mater 104:259–273

[21] Han J, Vitek V, Srolovitz DJ (2017) The grain-boundary structural unit model redux. Acta Mater 133:186–199

[22] Frolov T, Setyawan W, Kurtz RJ, Marian J, Oganov AR, Rudd RE, Zhu Q (2018) Grain boundary phases in bcc metals. Nanoscale 10:8253–8268

[23] Zhu Q, Samanta A, Li B, Rudd RE, Frolov T (2018) Predicting phase behavior of grain boundaries with evolutionary search and machine learning. Nat Commun 9:467

[24] Saylor DM, Morawiec A, Rohrer GS (2003) Distribution of grain boundaries in magnesia as a function of five macroscopic parameters. Acta Mater 51:3663–3674

[25] Saylor DM (2004) Distribution of grain boundaries in SrTiO3 as a function of five macroscopic parameters. J Am Ceram Soc 87:670–676

[26] Kim CS, Hu Y, Rohrer GS, Randle V (2005) Five-parameter grain boundary distribution in grain boundary engineered brass. Scripta Mater 52:633–637

[27] Wolf D (1990b) Structure-energy correlation for grain boundaries in f.c.c. metals-IV Asymmetrical twist (general) boundaries. Acta Metall Mater 38:791–798

[28] Tschopp MA, McDowell DL (2007a) Structures and energies of $\Sigma 3$ asymmetric tilt grain boundaries in copper and aluminium. Philos Mag 87:3147–3173

[29] Tschopp MA, McDowell DL (2007b) Asymmetric tilt grain boundary structure and energy in copper and aluminium. Philos Mag 87:3871–3892

[30] Brown JA, Mishin Y (2007) Dissociation and faceting of asymmetrical tilt grain boundaries: molecular dynamics simulations of copper. Phys Rev B 76:134118

[31] Olmsted DL, Foiles M, Holm EA (2009) Survey of computed grain boundary properties in face-centered cubic metals: I. Grain boundary energy. Acta Mater 57:3694–3703

[32] Medlin DL, Hattar K, Zimmerman JA, Dbdeljawad F, Foiles SM (2017) Defect character at grain boundary facet junctions: analysis of an asymmetric $\Sigma = 5$ grain boundary in Fe. Acta Mater 124:383–396

[33] Olmsted DL, Holm EA, Foiles M (2009) Survey of computed grain boundary properties in face-centered cubic metals: II. Grain boundary mobility. Acta Mater 57:3704–3713

[34] Zhang L, Lu C, Tieu K (2014) Atomistic simulation of tensile deformation behavior of $\Sigma 5$ tilt grain boundaries in copper bicrystal. Sci Rep 4:5919

[35] Duffy DM, Tasker PW (1983a) Computer simulation of <001> tilt grain boundaries in nickel oxide. Philos Mag A 47:817–825

[36] Duffy DM, Tasker PW (1983b) Computer simulation of <011> tilt grain boundaries in nickel oxide. Philos Mag A 48:155–162

[37] Oba F, Ohta H, Sato Y, Hosono H, Yamamoto T, Ikuhara Y (2004) Atomic structure of [0001]-tilt grain boundaries in ZnO: a high-resolution TEM study of fiber-textured thin films. Phys Rev 70:125415

[38] Browning ND, Chisholm MF, Pennycook SJ, Norton DP, Lowndes DH (1993) Correlation between hole depletion and atomic structure at high-angle grain boundaries in $YBa_2Cu_3O_{7-\delta}$. Physica C 212:185–190

[39] Lee SB, Sigle W, Rühle M (2003) Faceting behavior of an asymmetric $SrTiO_3$ $\Sigma 5$ [001] tilt grain boundary close to its defaceting transition. Acta Mater 51:4583–4588

[40] Lee SB, Lee JH, Cho YH, Kim D-Y, Sigle W, Phillip F, van Aken PA (2008) Grain-boundary plane orientation dependence of electrical barriers at $\Sigma 5$ boundaries in $SrTiO_3$. Acta Mater 56:4993–4997

[41] Lee H-S, Mizoguchi T, Yamamoto T, Kang SJL, Ikuhara Y (2011) Characterization and atomic modeling of an asymmetric grain boundary. Phys Rev B 84:195319

[42] Bean JJ, Saito M, Fukami S, Sato H, Ikeda S, Ohno H, Ikuhara Y, McKenna KP (2017) Atomic structure and electronic properties of MgO grain boundaries in tunneling magnetoresistive devices. Sci Rep 7:45594

[43] Plimpton S (1995) Fast parallel algorithms for short-range molecular dynamics. J Comp Phys 117:1–19

[44] Landuzzi F, Pasquini L, Giusepponi S, CelinoM MA, Palla PL, Cleri F (2015) Molecular dynamics of ionic self-diffusion at an MgO grain boundary. J Mater Sci 50:2502–2509. https://doi.org/10.1007/s10853-014-8808-9

[45] Yokoi T, Arakawa Y, Ikawa K, Nakamura A, Matsunaga K (2020) Dependence of excess vibrational entropies on grain boundary structures in MgO: a first-principles lattice dynamics. Phys Rev Mater 4:026002